

A unique oxygen ligand environment facilitates water oxidation in hole-doped IrNiO_x core-shell electrocatalysts

Hong Nhan Nong^{1,2}, Tobias Reier¹, Hyung-Suk Oh¹, Manuel Gliech¹, Paul Paciok³, Thu Ha Thi Vu⁴, Detre Teschner^{2,5}, Marc Heggen³, Valeri Petkov⁶, Robert Schlögl⁵, Travis Jones^{5*} and Peter Strasser^{1,7*}

The electro-oxidation of water to oxygen is expected to play a major role in the development of future electrochemical energy conversion and storage technologies. However, the slow rate of the oxygen evolution reaction remains a key challenge that requires fundamental understanding to facilitate the design of more active and stable electrocatalysts. Here, we probe the local geometric ligand environment and electronic metal states of oxygen-coordinated iridium centres in nickel-leached IrNi@IrO_x metal oxide core-shell nanoparticles under catalytic oxygen evolution conditions using operando X-ray absorption spectroscopy, resonant high-energy X-ray diffraction and differential atomic pair correlation analysis. Nickel leaching during catalyst activation generates lattice vacancies, which in turn produce uniquely shortened Ir–O metal ligand bonds and an unusually large number of *d*-band holes in the iridium oxide shell. Density functional theory calculations show that this increase in the formal iridium oxidation state drives the formation of holes on the oxygen ligands in direct proximity to lattice vacancies. We argue that their electrophilic character renders these oxygen ligands susceptible to nucleophilic acid-base-type O–O bond formation at reduced kinetic barriers, resulting in strongly enhanced reactivities.

Electrocatalytic oxidation of water is expected to play an important role in the development of energy conversion and storage technologies, since it provides electrons to reduce water to hydrogen, or carbon dioxide to carbon-containing fuels^{1,2}. One of the biggest challenges remaining in the electrocatalytic oxidation of water (the oxygen evolution reaction (OER)) is the exploration of a highly active, cost-effective and stable catalyst^{3–5}. To date, iridium oxide is by far one of the most appropriate OER catalysts, combining excellent activity and stability, especially in acidic media^{6,7}. Unfortunately, iridium is extremely scarce with tenfold smaller abundance than platinum⁸. Therefore, to facilitate the application of iridium as an OER electrocatalyst on a large scale, the required amount of iridium must be minimized without reducing the OER activity. Recently, we demonstrated that metal oxide hybrid core-shell IrNi@IrO_x nanoparticles⁹ show not only improved utilization of iridium but also significantly enhanced intrinsic activity for OER. In these types of nanoparticles, the non-noble metal (nickel) was deliberately leached out during an electrochemical pretreatment to form the active catalyst phase. Following this concept, recent studies of Ir–Ni mixed oxides¹⁰, and subsequently an IrO_x/SrIrO₃ catalyst¹¹, also showed that the depletion of non-noble metal (nickel and strontium, respectively) species leads to a significant increase in OER activity. For alloyed bimetallic electrocatalysts, the electrocatalytic activity could be improved due to strain effects, which alter the electronic structure of the active sites^{12–15}. However, for IrNi@IrO_x nanoparticles, despite their advances, the effects of deliberate non-noble

metal dissolution on the local atomic structure of the disrupted surface iridium centres and the nature of the actual catalytic sites have remained poorly understood. To clarify these important questions, we explored the geometric and electronic structure of IrNi@IrO_x core-shell nanoparticles under catalytic operating conditions.

To understand how the depletion of nickel and the resulting ligand environment of Ir sites in IrNi@IrO_x nanoparticles benefit the kinetic rate of OER, including enhancing the intrinsic and mass-based activity, the OER mechanism and active catalytic sites need to be determined at the atomic level. For pure iridium oxide, it has been claimed that the OER proceeds through a deprotonation mechanism^{16,17} where the hydroxide is converted into oxide on the catalytic surface at elevated potential. The highest iridium oxidation state in pure iridium oxides observed under OER conditions was $v+$, although the existence of Ir^{*v*+} in aqueous environments during the OER continues to be debated^{17–20}. In the present work, we uncover the electronic states and local geometric structures of catalytically active surface IrO_x centres in both Ir@IrO_x core-shell nanoparticles (hereafter referred to as IrO_x) and IrNi@IrO_x core-shell nanoparticles (hereafter referred to as IrNiO_x) using operando X-ray absorption spectroscopy (XAS). Complementary resonant high-energy X-ray diffraction (HE-XRD) experiments were also carried out at the K edge of iridium to reveal both the long-range atomic ordering and iridium-specific differential atomic pair correlations in these materials. We discuss the mechanistic origin of the OER activity enhancement in light of the unique oxygen ligand

¹Department of Chemistry, Chemical Engineering Division, Technical University Berlin, Berlin, Germany. ²Max Planck Institute for Chemical Energy Conversion, Mülheim an der Ruhr, Germany. ³Ernst-Ruska Center for Microscopy and Spectroscopy with Electrons, Forschungszentrum Jülich, Jülich, Germany. ⁴National Key Laboratory for Petrochemical and Refinery Technologies, Vietnam Institute of Industrial Chemistry, Hanoi, Vietnam. ⁵Department of Inorganic Chemistry, Fritz Haber Institute of the Max Planck Society, Berlin, Germany. ⁶Department of Physics, Central Michigan University, Mount Pleasant, MI, USA. ⁷Ertl Center for Electrochemistry and Catalysis, Gwangju Institute of Science and Technology, Gwangju, Republic of Korea. *e-mail: trjones@fhi-berlin.mpg.de; pstrasser@tu-berlin.de

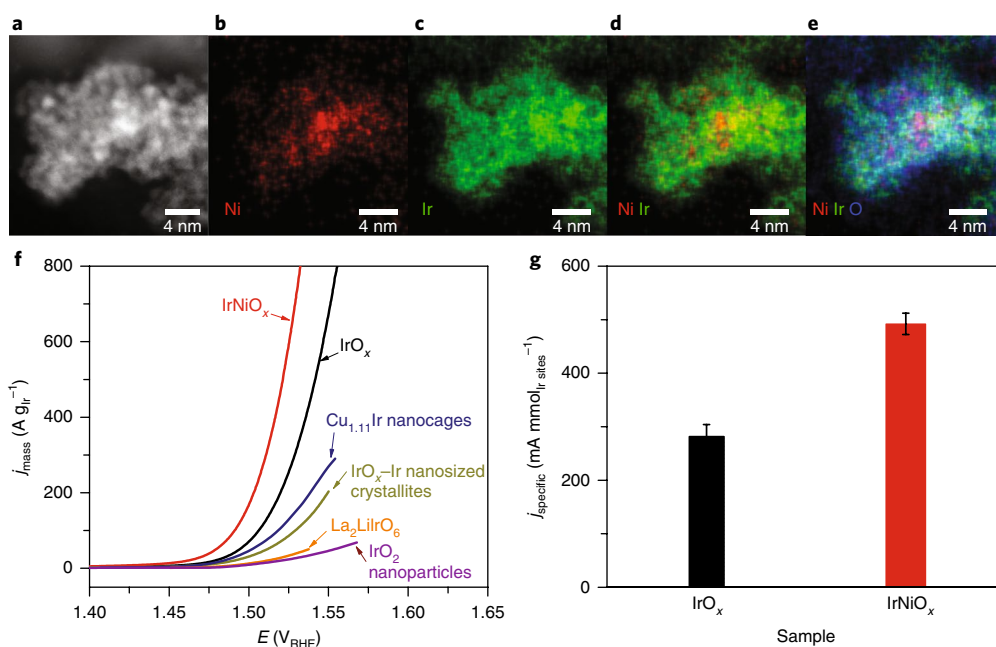


Fig. 1 | Morphology and catalytic OER activity of pure IrO_x and IrNiO_x core-shell nanoparticles. **a–e**, High-angle annular dark field STEM image (**a**) and corresponding EDX maps (**b–e**) of an IrNiO_x nanoparticle. Nickel, iridium and oxygen are displayed in red, green and blue, respectively. TEM images of iridium and IrNi_x nanoparticles can be found in Supplementary Fig. 1a,b. **f**, Iridium-mass-based OER activities (j_{mass}) in acidic electrolyte of IrO_x and IrNiO_x nanoparticles compared with state-of-the-art iridium catalysts from the literature. Data were adapted from ref. ²¹ for IrO_2 nanoparticles (purple), ref. ²² for $\text{Cu}_{1,11}\text{Ir}$ nanocages (blue), ref. ²³ for IrO_x -Ir nanosized crystallites (dark yellow) and ref. ²⁴ for $\text{La}_2\text{LiIrO}_6$ (orange). The polarization curves of IrO_x and IrNiO_x were iR and capacitance corrected. All polarization curves were obtained at a scan rate of 5 mV s^{-1} , except for the IrO_2 nanoparticles and $\text{La}_2\text{LiIrO}_6$ (10 mV s^{-1}). **g**, Specific surface active site-normalized activities (j_{specific}) of IrO_x and IrNiO_x at 300 mV overpotential. Error bars represent s.d. values obtained from three independent measurements. The electrochemical measurement conditions were: $0.05 \text{ M H}_2\text{SO}_4$, iridium loading: $10.2 \mu\text{g cm}^{-2}$.

environment of catalytically operating surface $\text{Ir}^{\text{N}+}$ sites in IrNiO_x . We show that, after the leaching of nickel, the sites exhibit significantly more *d*-band holes and unusually short Ir–O bond lengths compared with IrO_x and rutile-type IrO_2 , in which Ir sites have a formal oxidation state of IV+. With the support of density functional theory (DFT) calculations, we suggest that the initial presence and subsequent leaching of nickel from the near-surface region of the nanoparticles introduces a large number of lattice vacancies in the IrO_x shell and results in oxygen hole doping of the respective sites; that is, the appearance of oxygen $2p$ holes and the generation of electrophilic oxygen (formally $\text{O}^{\cdot-}$ ions) on the surface of IrNiO_x . Rapid O–O bond formation due to nucleophilic attack on iridium-bonded $\text{O}^{\cdot-}$ oxygen ligands can account for the greatly enhanced OER reactivity of IrNiO_x compared with IrO_x .

Results

Morphology and catalytic OER activity of pure IrO_x and IrNiO_x core-shell nanoparticles. IrO_x and IrNiO_x core-shell nanoparticle catalysts were prepared from the corresponding iridium and $\text{IrNi}_{3,2}$ nanoparticle precursors (see Methods and Supplementary Methods) using concomitant voltammetric dealloying and surface oxidation⁹. A typical high-angle annular dark field image and energy dispersive X-ray (EDX) maps of an individual IrNiO_x nanoparticle (Fig. 1a–e) confirm the core-shell structure of the nanoparticle with an IrO_x -rich shell. The nanoparticle exhibits an irregular, grainy IrO_x shell due to nickel leaching. Complementary to EDX mapping, operando XAS and resonant HE-XRD with extensive three-dimensional (3D) modelling, as discussed later, unambiguously demonstrate the metallic core–oxide shell structure of the IrNiO_x nanoparticles. The average composition is around 90 at% for iridium and 10 at% for nickel. More detailed transmission electron microscopy (TEM) images of the nanoparticle catalysts are shown in Supplementary Fig. 1a,b.

Figure 1f,g shows the OER activities normalized by the weight of iridium (that is, the iridium-mass-based activities, j_{mass}) and to the number of electrochemically accessible iridium sites (that is, the intrinsic specific activities, j_{specific})⁹, respectively (see Supplementary Methods), evidencing the high OER activity of the IrO_x and IrNiO_x catalysts. To put the performance of the present system into perspective, j_{mass} scans of today's state-of-the-art iridium-based electrocatalysts^{21–24} are included in Fig. 1f. For clarity, we prefer iridium-mass-based activities, not only because they are relevant for cost considerations of water electrolyzers, but also because evaluating and comparing published active surface areas or active bulk volumes of IrO_x catalysts has remained notoriously difficult and inaccurate^{9–11,25,26}. The reason is that no consensus on an experimental metric for the number of catalytically active sites of iridium-based electrocatalysts has been reached. In particular, the atomic force microscopy-based surface¹¹, TEM image-based area²¹, integrated anodic charge^{10,25} and number of $\text{Ir}^{\text{III}/\text{IV}+}$ sites^{9,23} have all been considered as measures of OER active surface area. In this study, we consider the number of electrochemically accessible $\text{Ir}^{\text{III}/\text{IV}+}$ sites as an upper bound of the OER active sites, according to previous studies of electrochemically prepared iridium oxides^{9,23}. Clearly, the present nickel-leached IrNiO_x catalyst outperformed the IrO_x nanoparticles and—by a large amount—other nanosized iridium oxide catalysts. Compared with rutile-type IrO_2 nanoparticles²¹, our IrNiO_x nanoparticles are 25 times more active on an iridium mass basis at +1.53 V versus a reversible hydrogen electrode (V_{RHE}) in $0.05 \text{ M H}_2\text{SO}_4$. IrNiO_x also exceeds IrO_x nanoparticles in terms of specific OER activities. At 300 mV overpotential (+1.53 V_{RHE}), the specific OER activity of IrNiO_x is around 1.7 times higher than that of IrO_x nanoparticles (Fig. 1g).

Electronic structure of iridium centres. To gain insight into the electronic structure of IrO_x and IrNiO_x core-shell catalysts, we

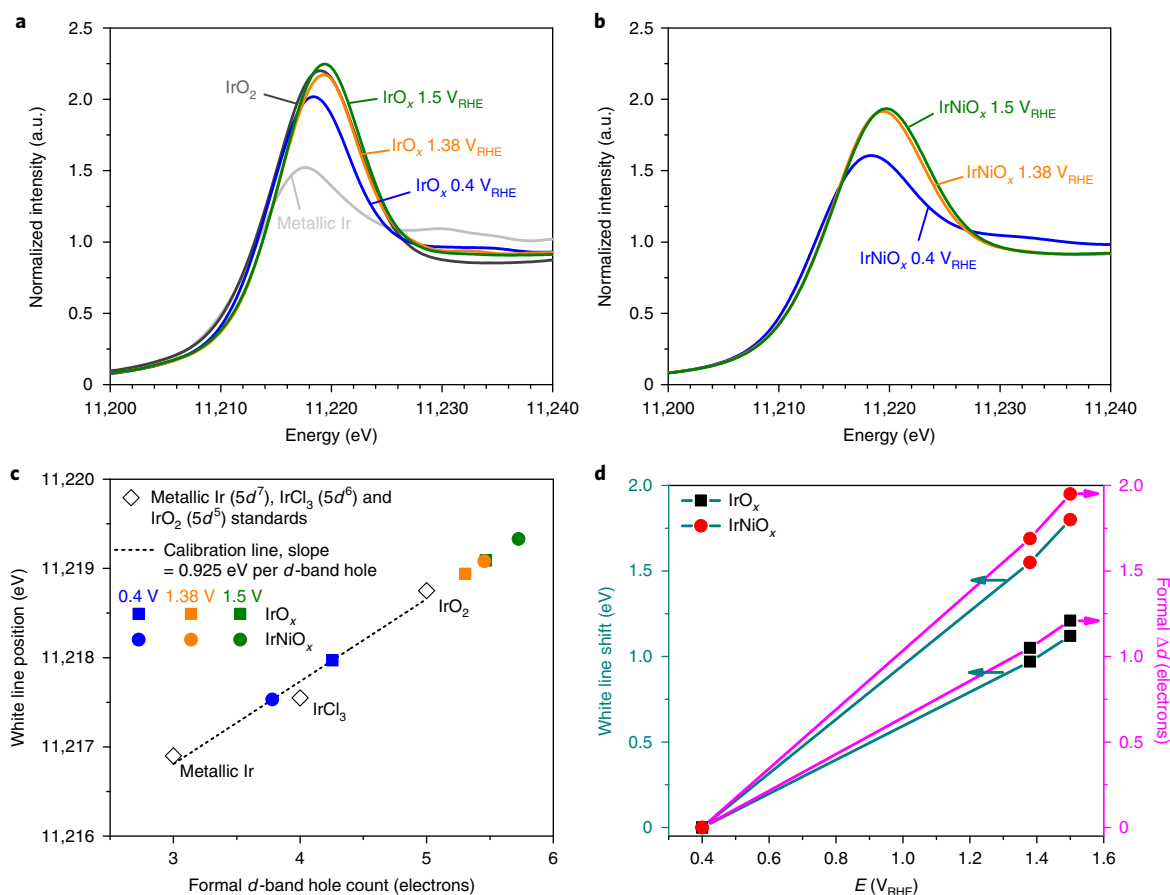


Fig. 2 | Electronic structure of iridium centres in IrO_x and IrNiO_x core-shell nanoparticles. **a,b**, Iridium L_3 -edge XANES region of IrO_x (**a**) and IrNiO_x (**b**) nanoparticles measured at different electrode potentials. XANES of metallic iridium and IrO_2 are shown in (**a**) as references. **c**, White line position of IrO_x (squares) and IrNiO_x (circles) as a function of the formal d -band hole count. Formal Δd values were calculated based on the white line shift and the increase of 0.925 eV per d -band hole calibrated from metallic iridium ($5d^7$), IrCl_3 ($5d^6$) and IrO_2 ($5d^5$) standards. **d**, Energy shift of the white line positions and formal Δd in IrO_x and IrNiO_x nanoparticles at different electrode potentials compared with the corresponding sample at $0.4 \text{ V}_{\text{RHE}}$.

performed X-ray absorption near-edge structure (XANES) measurements at the iridium L_3 edge. The iridium L_3 -edge XANES of IrO_x and IrNiO_x (Fig. 2a,b, respectively) are characterized by broad white lines, which primarily correspond to transition from occupied $2p$ to empty $5d$ states^{27–29}.

Figure 2c shows the white line position of the catalysts at different applied potentials as a function of the formal d -band hole count (see Methods for more details of XANES measurements and analysis) using a slope of 0.925 eV per d -band hole obtained from iridium ($5d^7 6s^2$), IrCl_3 ($5d^6 6s^0$) and IrO_2 ($5d^5 6s^0$) standards. Note that our derived slope is in excellent agreement with literature values^{18,19,30}. Mo et al.¹⁸ observed a total energy shift of around 1 eV over the potential range, which encompasses the $\text{Ir}^{\text{III}/\text{IV}}$ redox process. Hillman et al.¹⁹ also reported an energy shift of 1 eV per unit change in the iridium charge state; high valent iridium (Ir^{IV} , Ir^{V} and Ir^{VI}) compounds³⁰ have a mean energy shift of 1.077 eV per d -band hole (see Supplementary Fig. 6a). At $+0.4 \text{ V}_{\text{RHE}}$, the absolute number of d -band holes in IrO_x is between those of the IrCl_3 and IrO_2 standards. Based on established iridium electrochemistry^{16,31–35}, we expect to see Ir^{III} and/or Ir^{IV} sites at this potential for both the IrO_x and IrNiO_x samples. In fact, linear combination fitting³⁶ of the IrO_x and IrNiO_x XANES regions at $+0.4 \text{ V}_{\text{RHE}}$ (see Supplementary Fig. 6b) confirmed the coexistence of Ir^{III} and Ir^{IV} in both samples at such a low electrode potential, along with a small contribution of the Ir^0 core (12.5%) to the XANES region of IrO_x . For IrNiO_x , the larger contribution from the metallic Ir^0 core (61.1%) actually

depressed the experimentally observed average number of d -band holes below that of IrO_x . When the applied potential was increased from 0.4 to $1.38 \text{ V}_{\text{RHE}}$, the white line position of IrO_x and IrNiO_x shifted to higher energy due to the oxidation of iridium sites, as observed in the cyclic voltammogram (Supplementary Fig. 1d).

With XANES being a bulk-sensitive analytical technique, the white line energies still represent average values of the oxidized iridium atoms in the shell and the metallic iridium atoms in the particle bulk. As a result, the blue shift (upshift) of the white line energy on formation of the iridium oxide shell appears smaller for larger nanoparticles, where the contribution of the metallic bulk remains pronounced. This is why, to exclude the influence of the metallic cores on the white line energy shifts of the oxidic shells, we considered the white line energy differences (referred to as white line shifts in Fig. 2d) of IrO_x and IrNiO_x between $+1.38 \text{ V}_{\text{RHE}}$, $+1.5 \text{ V}_{\text{RHE}}$ and the reference potential $+0.4 \text{ V}_{\text{RHE}}$. This type of analysis is accurate because when the electrode potential is stepped and held at a constant value, the growth of oxide layers on iridium electrodes, which occurs layer by layer during potential cycling, does not proceed much further inside the nanoparticles^{31,37,38}. The results provide evidence that, while the white lines of both IrO_x and IrNiO_x nanoparticles shift to higher energies with an increase in the applied potential, the slope of the white line shift for IrNiO_x is significantly larger, indicating a more rapid increase with the potential compared with IrO_x . We are aware that the experimental uncertainty of the XANES measurements can influence the determination of the

white line shift, but by using the fluorescence–transmission geometry and metallic iridium as a reference for energy alignment (see Supplementary Fig. 2), any systematic energy drifts over the course of the measurements can be ruled out.

To learn about the electronic structure, we correlated the relative white line shifts with changes in the formal number of iridium *d*-band holes (Δd) in IrO_x and IrNiO_x at the two higher electrode potentials with respect to the number at $+0.4 \text{ V}_{\text{RHE}}$ (Fig. 2d) using the 0.925 eV per *d*-band hole slope. Data in Fig. 2d clearly shows that iridium *d* states in IrNiO_x nanoparticles depopulate much more rapidly with electrode potential than those in IrO_x . Given the coexistence of Ir^{III} and Ir^{IV} sites in both IrO_x and IrNiO_x at $+0.4 \text{ V}_{\text{RHE}}$, the experimentally observed Δd of 1.21 holes for IrO_x at $+1.5 \text{ V}_{\text{RHE}}$ is consistent with the generation of formal Ir^{IV} and Ir^{V} sites in IrO_x under OER conditions. However, more importantly, the much larger Δd of 1.95 holes for IrNiO_x suggests formal oxidation states approaching Ir^{VI} in the nickel-leached oxidic particle shell under operando oxygen evolution conditions. Even though there is no unanimous consensus on whether redox states above the absolute value of Ir^{IV} are sustainable in aqueous solutions, we can unequivocally conclude that nickel-depleted IrNiO_x nanoparticles exhibit significantly increased *d*-band holes (hence, formally higher iridium chemical redox states) during the OER than IrO_x nanoparticles or crystalline rutile-type IrO_2 . In other words, the electrochemical removal of nickel atoms from the surface of IrNiO_x nanoparticles and the concomitant electro-oxidation of iridium atoms generates a catalytically highly active type of iridium oxide in the particle shells with a uniquely high number of *d*-band holes. Based on their electronic fingerprint, we will refer to this surface IrO_x phase as hole-doped IrO_x .

Local geometric structure around iridium metal centres. To investigate the local geometric structure and ligand environment around iridium sites, we performed extended X-ray absorption fine structure (EXAFS) measurements and EXAFS simulations. The simulations of EXAFS spectra (Fig. 3a,b and Supplementary Table 1) revealed the presence of characteristic Ir–O bond distances in the oxidic particle shells and Ir–M ($M = \text{Ir}$ or Ni) distances in the metallic cores, confirming the metal oxide hybrid core–shell structures of both IrO_x and IrNiO_x .

To track the immediate coordination environment of our catalysts under OER conditions, Fig. 3c shows the evolution of Ir–O bond distances in both IrO_x and IrNiO_x with the applied electrode potential. It is common that transition metal–oxygen bond distances decrease with increasing redox state of the central metal ion^{30,39} because its effective ionic radius decreases. However, when stepping from $+0.4$ to $+1.38 \text{ V}_{\text{RHE}}$, the Ir–O distances for each sample remain comparable, although iridium attains higher redox states (see discussion above). This observation can be explained based on characteristic differences in the iridium ligands, which range from oxo (O), hydroxo (OH) to aqua (OH_2). In anodic IrO_x films prepared by potential cycling metallic iridium films in an acidic environment—similar to the electrochemical protocol applied for the nanoparticles in this study—hydroxo species are dominant at low electrode potential ($+0 \text{ V}$ versus the saturated calomel electrode (V_{SCE}) or $+0.24 \text{ V}_{\text{RHE}}$). The species undergo deprotonation to oxo species at higher electrode potential ($+0.9$ and $+1.25 \text{ V}_{\text{SCE}}$, or $+1.14$ and $+1.49 \text{ V}_{\text{RHE}}$, respectively), while aqua ligands seem to have no strong interaction with the surface¹⁶. The theoretical Ir–OH distance is shorter than the theoretical Ir–O distance if the iridium oxidation state and coordination number remain the same⁴⁰. In fact, the coordination numbers are comparable at the three electrode potentials (see Supplementary Table 1); therefore, the deprotonation of hydroxo to oxo ligands offsets redox state effects on bond lengths, thus accounting for the nearly constant Ir–O bond distance in IrO_x and IrNiO_x during iridium oxidation between $+0.4$ and $+1.38 \text{ V}_{\text{RHE}}$. The observed Ir–O bond lengths in the IrO_x nanoparticles are in

good quantitative agreement with other in situ EXAFS studies on IrO_x films and IrO_2 nanoparticles^{18,19,41}. In contrast, unusually short Ir–O bond lengths in the shells of IrNiO_x nanoparticles, in particular under conditions of oxygen evolution at $+1.5 \text{ V}_{\text{RHE}}$, were observed.

To emphasize the correlation of the electronic and geometric structures of IrO_x and IrNiO_x , Fig. 3d shows Ir–O bond distances in IrO_x and IrNiO_x nanoparticles as a function of the formal *d*-band hole count, together with previously reported Ir–O distances in IrO_x films^{18,19}. Theoretical Ir–O and Ir–OH distances (dotted and dashed lines) computed from the effective ionic radii of $\text{Ir}^{\text{N+}}$ ions with $\text{O}^{\text{m-}}$ or $\text{OH}^{\text{-}}$ ions⁴⁰ (see Supplementary Methods) are also shown as references. The Ir–O distances in IrO_x follow predicted Ir–OH and Ir–O distances very well, supporting the XANES results; that is, that Ir^{III} and Ir^{IV} sites are present in IrO_x at $+0.4 \text{ V}_{\text{RHE}}$ and then oxidized to Ir^{IV} (and some higher formal oxidation state) at $+1.5 \text{ V}_{\text{RHE}}$. At $+0.4 \text{ V}_{\text{RHE}}$, experimental values of the Ir–O distance in IrNiO_x indicate the presence of Ir^{III} and Ir^{IV} sites similar to IrO_x , although the determined mean number of *d*-band holes in IrNiO_x is lower due to the influence of the metallic cores. For reference, Ir–O distance in our IrO_2 standard is in excellent agreement with Ir–O distance calculated for Ir^{IV} (formally five *d*-band holes), as well as with literature values^{42,43}. Note that Ir–O distances in IrO_x films reported by Mo et al.¹⁸ and Hillman et al.¹⁹ are also in excellent agreement with the theoretically derived Ir–O and Ir–OH distances. The correlation between datasets in Fig. 3d testifies to the very unusual oxygen ligand environment of iridium centres in the shell of IrNiO_x nanoparticles. In particular, our data reveal substantially shorter Ir–O bond lengths (1.91 Å) in nickel-leached electrochemical oxide particle shells compared with conventional iridium oxides^{18,19,41}. This short Ir–O bond is consistent with the concept of a covalency contraction, as defined by Shannon and Vincent⁴⁴. A parameter R_d —defined for transition metal halogens and chalcogens as the cube of the mean M–X bond length (R_d) relative to that of Mg_mX_n ⁴⁴—quantitatively accounts for bond shortening due to increasing covalency and is inversely proportional to the covalency of the M–X bond. R_d values for IrO_x and IrNiO_x under OER are 0.834 and 0.774, respectively, both of which are lower than that of rutile-type IrO_2 (0.869), suggesting that the covalency of the Ir–O bond increases in the order rutile-type $\text{IrO}_2 < \text{IrO}_x < \text{IrNiO}_x$.

We now turn to discussing the immediate oxygen environment of surface iridium atoms under catalytic OER conditions at $+1.5 \text{ V}_{\text{RHE}}$, where both IrO_x and IrNiO_x show shortened surface Ir–O bond lengths (Fig. 3c). In particular, while Ir–O distances in IrO_x appear contracted by 0.016 Å, those in IrNiO_x are shortened by 0.049 Å down to 1.91 Å, thus appearing as uniquely short, previously unreported Ir–O ligand bond distances. This observation calls for reconciliation with the electronic structure data discussed above. Choy et al.³⁰ reported (ex situ) a decrease in Ir–O bond distances corresponding to 0.039 Å per electron oxidation state change (or 0.039 Å per *d*-band hole) between Ir^{IV} , Ir^{V} and Ir^{VI} ions in perovskites. Geometric structure of Ir sites in perovskites might be different from that of Ir sites in IrO_2 and IrNiO_x . However, the bond distance change of 0.039 Å per *d*-band hole in iridium perovskites is entirely due to a change in the oxidation state of iridium sites, and not a change in the geometry of a framework of octahedral units centred by iridium atoms. We also exclude the effect of nickel on the bond distance in the IrO_x shell since nickel-substituted iridium oxides adopt a NiO rock-salt-type bunsenite structure¹⁰, wherein metal–oxygen bonding distances are longer than those in rutile-type IrO_2 . Thus, the extremely short Ir–O distance in IrNiO_x would again suggest a formal iridium redox state $> \text{Ir}^{\text{IV}}$. This picture is in line with the aforementioned XANES-based conclusions that surface iridium sites in IrNiO_x display a significantly higher number of *d*-band holes compared with IrO_x .

The link between the observed Ir–O bond lengths and change in *d*-band holes can be seen by way of DFT calculations (see Methods

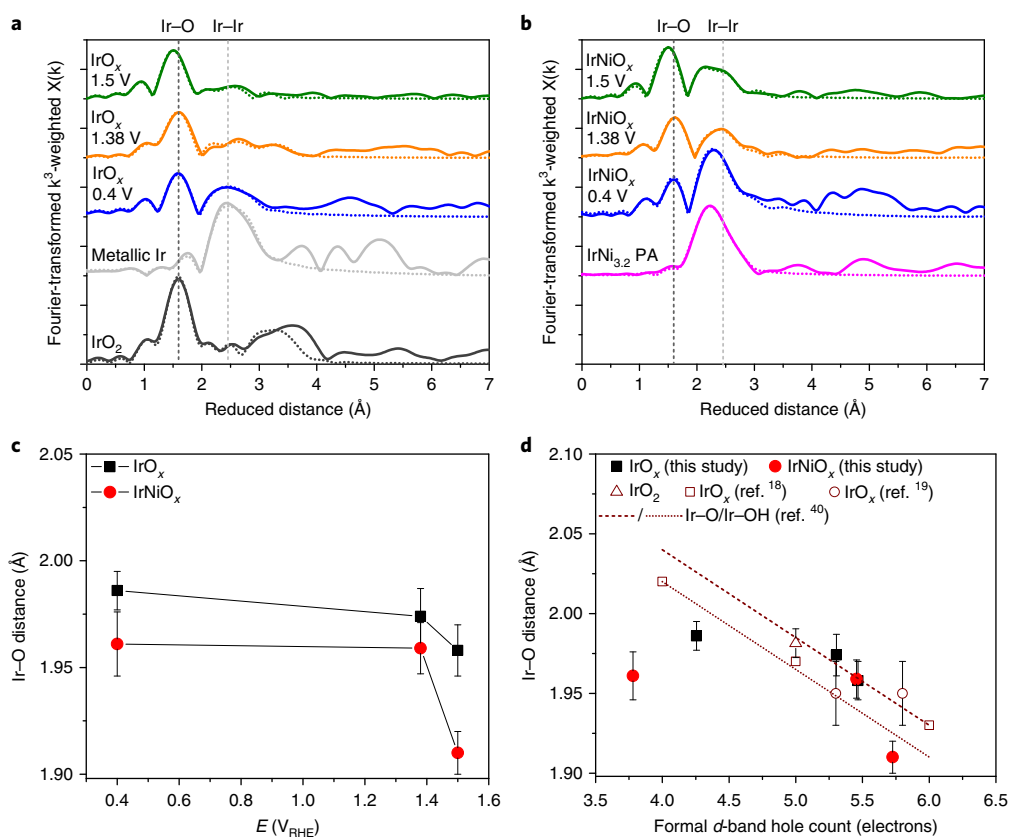


Fig. 3 | Local geometric structure of iridium centres in IrO_x and nickel-leached, lattice defect-rich IrNiO_x core-shell nanoparticles. **a, b**, k^3 -weighted Fourier transforms of EXAFS spectra collected at the iridium L_3 edge of the IrO_x (**a**) and IrNiO_x nanoparticles (**b**). Results for metallic iridium and rutile-type IrO_2 are included as standards in **a**, along with the $\text{IrNi}_{3.2}$ precursor alloy (PA) in **b**. Experimental data (solid lines) and fits (dotted lines) are shown. The potential (V_{RHE}) at which the EXAFS measurements were collected is given for each dataset. Vertical dashed lines indicate Ir–O and Ir–Ir reduced distances for the rutile-type IrO_2 and metallic iridium standards, respectively. **c**, Ir–O bond distances at different applied potentials. **d**, Experimental operando Ir–O bond distances versus the iridium d -band hole count for IrO_x and IrNiO_x nanoparticles from this study (solid black squares and solid red circles, respectively), as well as IrO_x films from previous studies (ref. ¹⁸, empty squares; and ref. ¹⁹, empty circles). The Ir–O distance in the rutile-type IrO_2 standard measured ex-situ in this study is included as reference. The dashed and dotted lines connect the Ir–O and Ir–OH distances, respectively, obtained from the effective ionic radii of Ir^{N+} ions ($N = \text{III, IV or V}$, corresponding to formal d -band hole counts of four, five or six, respectively) with O^{2-} or OH^- ions (ref. ⁴⁰). Error bars in **c** and **d** represent the uncertainties of the bond lengths obtained from the EXAFS simulations.

and Supplementary Methods for details). We computed a series of pristine bulk structures, including rutile-type IrO_2 and the hollandite and romanechite motifs recently observed in amorphous IrO_x samples⁴⁵, along with defect structures with varying numbers of iridium/nickel vacancies. Figure 4a shows the computed Δd of the iridium atoms plotted against their change in average computed Ir–O bond length compared with IrO_2 . The formally $\text{Ir}^{\text{III}}\text{OOH}$, which was recently synthesized⁴⁶ can be seen to have the longest average Ir–O bond and fewer d -band holes than rutile-type IrO_2 . All the other crystalline materials, including the hollandite and romanechite types, have a Δd near zero and a computed average Ir–O bond length near that of rutile-type IrO_2 . Introducing defects increases Δd of the iridium atoms near the metal vacancy while simultaneously decreasing the average Ir–O bond length. For the lowest density of metal vacancies, $\text{Ir}_{47}\text{O}_{96}$, Δd is less than 0.1 electron and the average Ir–O bond remains nearly unchanged compared with that in IrO_2 . At higher metal-vacancy densities (that is, Ir_7O_{16}), the average Ir–O bond length of the iridium atoms near the vacancy drops by nearly 0.02 \AA , consistent with the IrO_x samples investigated here, although Δd remains below 0.2 electron. It is not until the material becomes extremely defective—with a stoichiometry (Ir_3O_8) giving a similar Ir:O ratio to that found for an IrNiO_x nanoparticle shell by analysis of the HE-XRD data shown below—that the average Ir–O bond length drops to values observed for IrNiO_x , with a concomitant increase in Δd to ~ 0.3 – 0.4 electron.

The calculations also reveal a profound effect of these short Ir–O bonds on the ligands. To see this, we define (in analogy to Δd) Δp —the change in the oxygen hole character relative to oxygen in rutile-type IrO_2 (Fig. 4b), where only the oxygen atoms near the iridium vacancies are considered for the defect structures. At the lowest metal-vacancy density, where $\Delta d < 0.1$ electron, Δp on the oxygen atoms near the defect can reach 0.2 electron; that is, the oxygen is oxidized, becoming more electrophilic than in rutile-type IrO_2 . In the case of the highly defective structures, with an Ir_3O_8 stoichiometry, the short Ir–O bond length leads to increased orbital overlap and a Δp of 0.3 electron. This behaviour can also be seen in the projected density of states (PDOS), where, as the iridium vacancy density increases, the amount of iridium $5d$ and oxygen $2p$ character at $\sim 1 \text{ eV}$ above the Fermi energy grows (see Fig. 4c–e and Supplementary Fig. 9). In the most extreme case, the average Ir–O bond length reaches those observed for IrNiO_x , and the oxygen hole contribution to the ground state becomes so large that the unoccupied states just above the Fermi energy are a near-equal mix of oxygen $2p$ and iridium $5d$ (see Fig. 4e). This behaviour is shown quantitatively for the whole series of structures in Supplementary Fig. 9g.

While bond length contraction could lead to oxygen $2p$ hole formation, inspection of the occupied states suggests that a lowering of the iridium $5d$ states due to an increase in Δd might instead be responsible. The occupied PDOS values show that as the

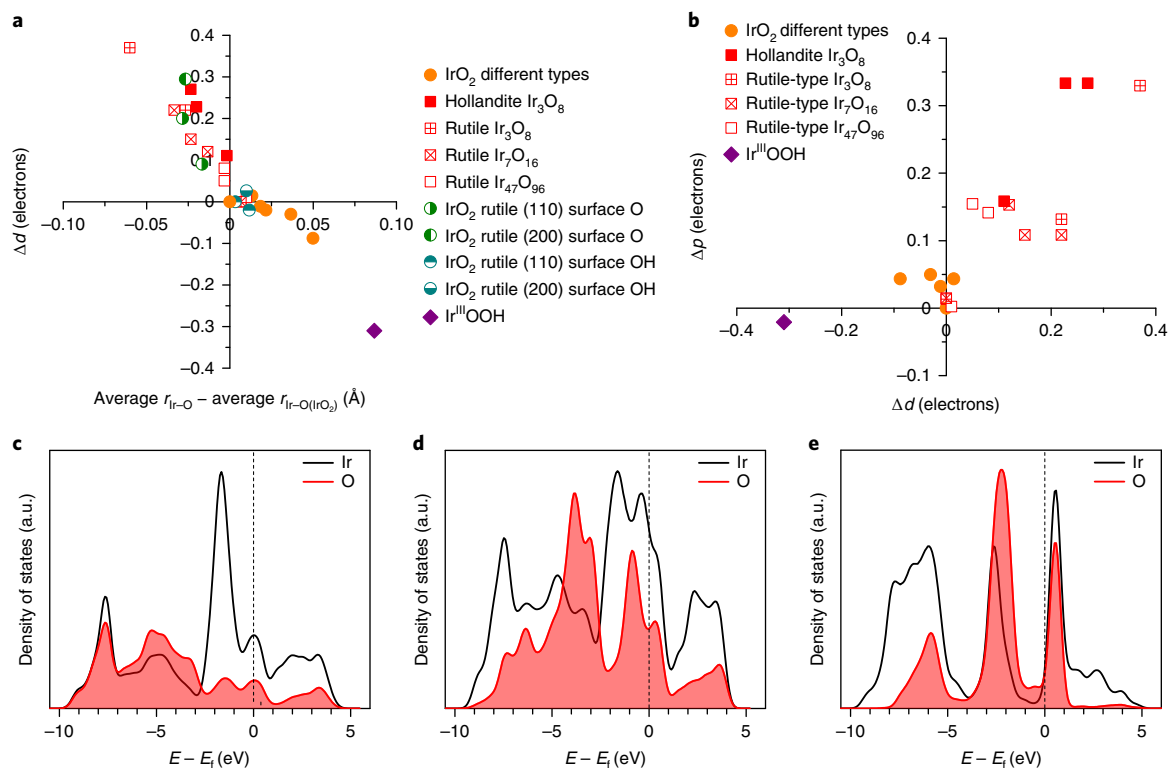


Fig. 4 | Computed electronic structure of iridium oxides with various metal-vacancy densities. **a**, Computed Δd of the iridium atoms plotted against their change in average computed Ir–O bond length compared with that in rutile-type IrO_2 . **b**, Computed Δp —the change in the oxygen hole character relative to oxygen in rutile-type IrO_2 —plotted against the computed Δd . **c–e**, Projected density of iridium $5d$ and oxygen $2p$ states for rutile-type IrO_2 (**c**), iridium and oxygen at an iridium vacancy in $\text{Ir}_{47}\text{O}_{96}$ (**d**) and iridium and oxygen in the vacancy-rich Ir_3O_8 (**e**). E , energy; E_f , energy of the Fermi level.

number of iridium vacancies increases, the character of the σ -bonding state at around -7 eV changes from equally mixed oxygen $2p$ and iridium $5d$ to strongly iridium $5d$. These changes are reminiscent of entering a negative charge-transfer or self-doped regime, where the metal d states lie below the oxygen $2p$ before hybridization⁴⁷. Such a situation would result in the appearance of ground-state oxygen holes—which we formally call O^{1-} or, more generally, $\text{O}^{(ii-\delta)-}$. We confirmed that the lowering of the iridium $5d$ states with increasing iridium vacancy concentration is sufficient to produce oxygen holes by computing the PDOS for the vacancy-rich structures without including atomic relaxation (see Supplementary Fig. 9h,i). Thus, the increase in Δd drives oxygen hole formation because it pushes the iridium $5d$ states below the oxygen $2p$.

Although highly active in OER, these hole-doped sites, formed as a result of nickel leaching, are also surprisingly stable. To examine their stability, we performed OER tests of the IrNiO_x nanoparticles after different numbers of oxidation potential cycles (10, 25, 50 and 75 cycles; Supplementary Fig. 1e). The OER activity increased with increasing numbers of oxidation cycles from 10 to 25 cycles, and remained unchanged when more oxidation cycles were applied (50 and 75 cycles), demonstrating that there is probably a dynamic equilibrium between defect healing and reformation. Prolonged leaching clearly generates more holes, leading to higher OER activity; however, the generation rate probably levels off once the majority of the near-surface nickel has leached, resulting in unchanged OER activity after 25 cycles of oxidation.

The remarkable stability of the nickel-leached particles under cycling may be rationalized when considering the reduction of the ligand holes. When the applied potential is lowered, the ligand hole sites are thermodynamically no longer stable and are reduced. Using the Ir_3O_8 stoichiometry as an example, our DFT calculations show that the four formally O^{1-} sites will be reduced to OH sites

at potentials below ~ 1.4 V versus the theoretical standard hydrogen electrode at pH 0 and 298 K⁴⁸. Once the ligand holes have been reduced, the nickel-leached vacancy sites will have been filled by OH formation, resulting in a metastable state that cannot easily be transformed into the more stable rutile-type oxide. This type of hydration has been used to explain the development of oxygen K-edge spectra of iridium foils under potential cycling⁴⁹, and in this example is predicted to lengthen the average Ir–O bond length of the hole-doped atoms to 1.91–2.02 Å depending on the number of reduced O^{1-} present, where the HIr_3O_8 stoichiometry has an average bond length of 1.91 Å and $\text{H}_4\text{Ir}_3\text{O}_8$ has an average bond length of 2.02 Å. This behaviour is in agreement with the observed changes in bond length after cycling, suggesting that the initial defect healing occurs largely through reversible hydration of the hole-doped sites.

Long-range order and element-specific atomic pair correlations.

In addition to operando XAS measurements, we performed complementary ex situ resonant HE-XRD experiments to investigate distinct atomic pair distribution functions (PDFs) in iridium, $\text{IrNi}_{3,2}$ precursor nanoparticles, and IrO_x and IrNiO_x core-shell nanoparticles (see Methods and Supplementary Methods for more details on the resonant HE-XRD experiments and derivation of total and iridium differential atomic PDFs).

The total PDFs of iridium and $\text{IrNi}_{3,2}$ nanoparticles (Fig. 5a) fit well with a model based on a face-centred cubic (fcc)-type structure, indicating that the nanoparticles are single nanophase. The first peak in the PDF for pure iridium nanoparticles is positioned at about 2.70 Å, which is close to the bulk value of 2.71 Å. The slight contraction of Ir–Ir pair distances in pure iridium nanoparticles can be attributed to increased surface tension and other surface-related effects known to occur in metallic materials confined to nanoscale dimensions. Furthermore, the first peak in the PDF for

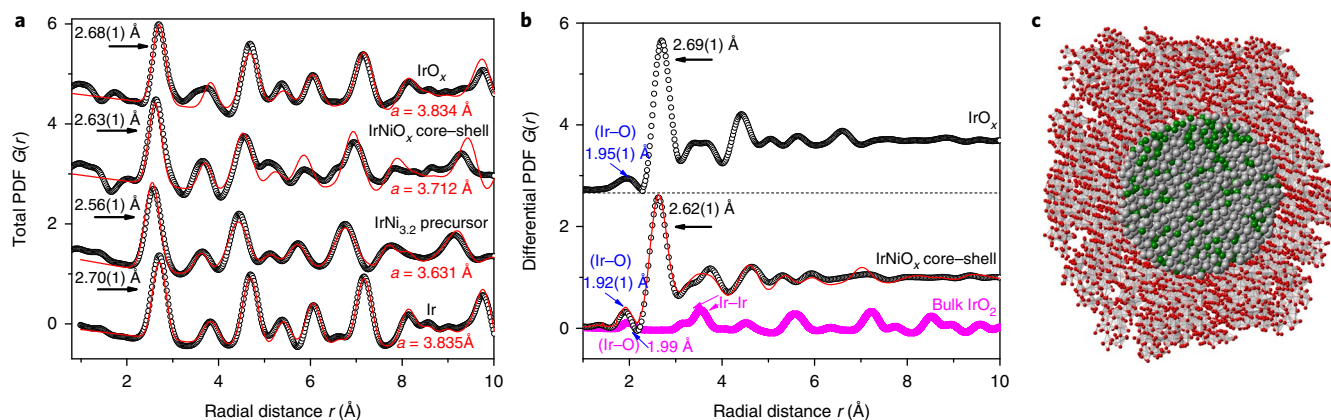


Fig. 5 | Long-range order, element-specific atomic pair correlations and a structure model. **a**, Experimental total atomic PDFs (symbols) for iridium, IrNi_{3.2} alloy, and the IrO_x and IrNiO_x nanoparticles. Arrows mark the position of the first PDF peak. Fits based on an fcc lattice model (red lines) and refined fcc lattice parameters (*a*) are also given for each dataset. **b**, Experimental differential PDFs (symbols) for the IrO_x and IrNiO_x nanoparticles. The computed PDF of IrNiO_x (red line) is derived from the 3D model shown in **c**. The model PDF for hypothetical rutile-type IrO₂ nanoparticles (magenta line) is also given. Black and magenta arrows mark the PDF peaks reflecting Ir–M (M = Ir or Ni) in the respective particles. Blue arrows mark the PDF peaks reflecting surface Ir–O atomic pair correlations. To emphasize the low-*r* atomic pair correlations, experimental and model PDF data in **b** are represented in terms of *g*(*r*), where *g*(*r*) = 1 + *G*(*r*)/(4π*r*ρ₀). **c**, 3D model of an IrNiO_x core-shell nanoparticle with a metallic IrNi alloy core and an iridium oxide shell. Oxygen atoms are shown in red, while iridium atoms centring Ir–O octahedra are shown in grey. Nickel and iridium atoms forming the metallic core are shown in green and grey, respectively. The model is approximately 9 nm × 6.5 nm × 5 nm in size.

pure IrNi_{3.2} nanoparticles is positioned at about 2.56 Å, reflecting the nanoalloy nature of the nanoparticles, wherein nickel (around 2.49 Å) and iridium (around 2.71 Å) atoms are intermixed. In contrast, total PDFs for IrO_x and IrNiO_x nanoparticles do not fit well with a model based on an fcc-type structure, known to occur with bulk nickel, iridium and Ir–Ni alloys. The poor fit indicates that, due to the electrochemical treatment, pure iridium and IrNi_{3.2} alloy nanoparticles have undergone near-surface phase segregation. In particular, the surface of iridium nanoparticles has probably undergone a partial oxidation, so the average first-neighbour distance in IrO_x nanoparticles appears shorter (around 2.68 Å) than in fresh iridium nanoparticles (2.70 Å). Furthermore, nickel atoms have probably leached from IrNi_{3.2} nanoparticles in large numbers; hence, the average first-neighbour distance in IrNiO_x nanoparticles appears longer (around 2.63 Å) than in fresh IrNi_{3.2} nanoparticles (around 2.56 Å). In addition, as revealed by the iridium differential PDFs (Fig. 5b), the nanoparticles have undergone significant surface oxidation. The presence of surface Ir–O species in both IrO_x and IrNiO_x nanoparticles is best revealed by the low radial distance (*r*) peaks in the respective iridium differential PDFs. On average, Ir–O bond distances in IrO_x and IrNiO_x nanoparticles appear at 1.95 and 1.92 Å, respectively. The distances are significantly shorter than those found in stoichiometric, rutile-type IrO₂ (around 1.99 Å).

A 3D model of an IrNiO_x particle (Fig. 5c and Supplementary Videos 1 and 2) was computed based on the iridium differential atomic PDF. The model is approximately 9 nm × 6.5 nm × 5 nm in size. It has a chemical composition of (Ir_{1,609}Ni₅₄₈)core (Ir_{3,766}O_{9,761})shell and is somewhat bent over a cylindrical surface with a radius of about 30 nm. The model reproduces the experimental iridium differential atomic PDF well (Fig. 5b). Note that all the iridium atoms from the IrO_x shell are sixfold coordinated by oxygen atoms, thus forming IrO₆ octahedra. The octahedra are linked together forming a continuous network riddled with iridium vacancies. Also note that the octahedra from the IrO_x shell appear rather distorted compared with those in stoichiometric rutile-type IrO₂.

Together, in line with the findings from the EXAFS experiments, iridium differential PDFs unambiguously show that due to electrochemical treatment: (1) IrNi_{3.2} nanoparticles have lost significant nickel content and are therefore partially (nano)phase segregated;

(2) both iridium and IrNi_{3.2} nanoparticles have undergone significant surface oxidation, thus becoming hybrid metal core–metal oxide shell nanoparticles; and (3) surface iridium centres and their oxygen ligands in the IrO_x and IrNiO_x nanoparticles exhibit a metal ligand environment with significantly contracted bond lengths. Point (3) is consistent with the presence of a significant number of vacancies in the clearly non-stoichiometric (non-rutile-type) IrO_x shell of the nanoparticles.

Figure 6 highlights our key findings for the surface atomic and electronic structures of IrO_x and IrNiO_x nanoparticles. It also illustrates our understanding of how nickel leaching leads to a high degree of covalency and ultimately shortens Ir–O bonds and affects the catalytic reactivity of the nanoparticles. The bar graph in Fig. 6a shows the changes in the experimental Ir–O metal ligand distances of a selected set of iridium-based catalysts under OER compared with the mean Ir–O distance in stoichiometric rutile-type IrO₂⁴². Notably, the Ir–O bond lengths in IrNiO_x nanoparticles display a unique contraction.

Figure 6b illustrates our hypotheses and findings of a relationship between geometric and electronic effects and OER activity in IrNiO_x. The figure displays the surface Ir–O metal ligand environment of IrNiO_x nanoparticles under catalytic OER conditions. In line with the results described above, nickel leaching causes the formation of iridium lattice vacancies, which (due to charge neutrality) constitute hole doping of the lattice. As a result, iridium ions adjacent to vacancies increase their hole character and take on oxidation states more positive than those in crystalline rutile-type IrO₂, formally IV⁺. This lowers the iridium 5*d* levels—below the oxygen 2*p* levels (Fig. 4) at vacancy densities consistent with the IrNiO_x nanoparticle shells prepared in this work—and leads to a self-doped material with significant oxygen hole character. That is, terminal electrophilic oxygen ligands, O^{(II-δ)-} (probably –O(H) or =O), are formed in response to the unusually large number of iridium *d*-band holes in the IrNiO_x nanoparticles. The hole character of the oxygen ligands is reflected in the emergence of a narrow band of unoccupied states ~1 eV above the Fermi level, which, due to the high degree of covalency, also has significant iridium character. In agreement with the high degree of covalency, the Ir–O bonds are contracted to uniquely short distances; in other words, the O^{(II-δ)-}

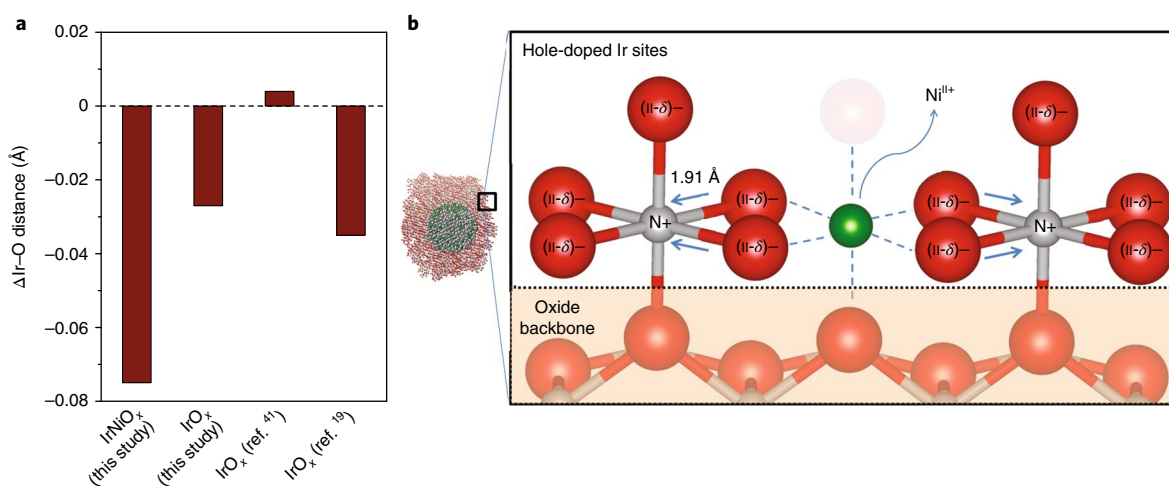


Fig. 6 | Iridium sites under OER in the nickel-leached IrO_x shell of IrNi@IrO_x core-shell nanoparticles. a, Changes in Ir–O distances of IrO_x nanoparticles, IrNiO_x nanoparticles, IrO_x film (ref. 19) and IrO₂ particles (ref. 41) relative to the theoretical mean Ir–O distance in bulk rutile-type IrO₂ (1.985 Å). **b**, Schematic of catalytic sites in IrNiO_x core-shell nanoparticles. Oxygen atoms are in red, iridium atoms are in grey and nickel atoms are in green. Nickel atoms were leached out during the electrochemical oxidation step, resulting in hole-doped IrO_x shells with electrophilic oxygen ligands surrounding *d*-band hole-doped Ir^{N+} sites. The schematic was created using the VESTA program⁵⁷.

ligands in catalytically operating IrNiO_x nanoparticle shells possess, on average, more electrophilic character than IrO_x nanoparticles or crystalline rutile-type IrO₂. The electrophilic nature affects the catalytic rate of O–O bond formation during the OER, which can proceed either via the acid–base mechanism or through a direct (or radical) coupling mechanism^{50,51}. In the acid–base mechanism, the O–O bond is formed via a nucleophilic attack of a water molecule or hydroxide ion on the metal-bound, electrophilic oxo species, whereas in the direct coupling mechanism two neighbouring oxygen-based radicals combine⁵⁰. Electrophilic oxygen ligands at hole-doped iridium sites in IrNiO_x facilitate O–O bond formation via a nucleophilic attack, resulting in higher site-specific activity compared with IrO_x. Our findings are in agreement with a differential electrochemical mass spectrometry study of an IrO₂ catalyst⁵², which showed that oxygen molecules indeed evolve from lattice oxygen. Our findings are also in agreement with a recent study^{20,49}, in which electrophilic oxygen, O^{(ii-δ)-}, was found to be responsible for the higher OER activity of X-ray amorphous IrO_x compared with crystalline IrO₂.

The issue of a competing redox activity of iridium centres and oxygen ligands in coordinative bonding with high covalent character has become a matter of debate. In an in situ XPS study of IrO₂, Sanchez Casalongue et al.¹⁷ assigned the iridium oxidation state *v+* to an iridium 4*f* core level peak 0.7 eV above that of Ir^{IV+}. Mo et al.¹⁸ and Hillman et al.¹⁹ also reported Ir^{V+} sites based on their in situ XANES studies. In contrast, ex situ oxygen K-edge studies of Ir–Ni mixed oxide revealed evidence of 2*p* holes on lattice oxygen before and after the catalytic reaction^{10,53}. Shortly after, Pfeifer et al.^{20,49} produced in situ oxygen K-edge XANES and DFT evidence of electrophilic O^{(ii-δ)-} species, based on their highly unusual electronic fingerprint resonance at 529 eV. However, direct chemical bond and geometric evidence of electrophilic surface oxygen species has been absent until now. What is more, the present study underlines the challenges associated with trying to quantitatively allocate hole character to either iridium centres or oxygen ligands, evidencing the presence of shared hole character due to the high degree of covalency. A key concept emerging from this work is that the strong covalent nature of the chemical bonding in amorphous and defective IrNiO_x leads to the formation of electrophilic oxygen ligands that are highly conducive for enhanced catalytic OER

activity by lowering kinetic barriers owing to the acid–base O–O formation process during the oxygen evolution cycle⁵.

In conclusion, our synthetic, electrochemical, operando XAFS and ex situ resonant HE-XRD studies and DFT calculations have probed the local geometric ligand environment and electronic metal states of oxygen-coordinated iridium centres in IrNiO_x core-shell nanoparticles. We have uncovered a number of unique structural and chemical features of this catalyst which advance our fundamental understanding of the reactivity of bimetallic core-shell iridium catalysts. First, we have provided experimental proof that the oxygen evolution reactivity of IrNiO_x nanoparticles, normalized to the mass of iridium in the particle catalyst, by far surpasses that of recently highlighted iridium-based OER catalysts^{21–24}. More importantly, based on operando XAS, supported by ex situ resonant HE-XRD data, we conclude that metal leaching from iridium oxide lattices results in the injection of a massive number of vacancies in the iridium oxide particle shell. As a result, the number of *d*-band holes on surface iridium centres reaches unusual positive values. DFT calculations show that concomitant lowering of the iridium 5*d* energy leads to an increase in the hole character on the oxygen ligands, resulting in the observed unusually short Ir–O metal ligand bond distances. The enhanced electrophilic character of these oxygen ligands makes them experience smaller kinetic barriers during OER catalysis due to an energetically favourable acid–base O–O bond formation mechanism involving the nucleophilic attack of a nucleophilic water molecule or hydroxyl ligand on the electrophilic oxygens. This makes the electrophilic oxygens the active catalytic sites. In a broader context, our present study suggests a quite general doping/dissolution strategy for more active OER catalysts, which is probably transferable to other transition metal oxides.

Methods

Synthesis of IrNi, bimetallic precursor alloy nanoparticles. IrNi_{3.2} precursor alloy nanoparticles were prepared using a previously reported modified polyol method⁹. Briefly, Ir(ac)₃ (Chempur; 48 wt% iridium) was injected to the reaction flask containing Ni^{II} acetate tetrahydrate (98%; Alfa Aesar), 1,2-tetradecanediol (90%; Sigma–Aldrich), oleylamine (70%; Sigma–Aldrich), oleic acid (99%; Alfa Aesar) and dibenzyl ether (99%; Alfa Aesar) at 240 °C. The bulk composition was controlled by adding an appropriate stoichiometric ratio of iridium and nickel precursors. After 1 h, the reaction was allowed to cool to room temperature. The

alloy nanoparticles were then supported on carbon (Vulcan XC-72R carbon black) with a target of 20 wt% iridium. To remove the remaining surfactants, ethanol-washed IrNi_{3.2} nanoparticles on carbon were annealed at 180 °C in synthetic air (25 vol% of O₂ and 75 vol% of N₂) for 2 h. Then, N₂ was purged into the furnace for 1 h at 180 °C to remove O₂. Afterwards, the catalyst powders were further annealed at 400 °C in H₂ for 4 h.

Synthesis of pure iridium nanoparticles. Pure iridium nanoparticles were synthesized using a previously reported polyol method³¹. In particular, Ir(CH₃COO)₃ was reduced in a 0.15 M solution of sodium hydroxide in ethylene glycol at 160 °C for 30 min. The pure iridium nanoparticles were then supported on carbon (Vulcan XC-72R carbon black) with a target of 20 wt% iridium. The received powder was heat treated at 250 °C under an N₂ atmosphere to remove the remaining organic substances. A detailed description of the synthesis procedure is provided in the Supplementary Methods.

Material characterization. The morphology and composition of the samples were investigated by TEM (FEI Tecnai G2 20 S-TWIN), scanning TEM (STEM) (FEI Titan ChemiSTEM) and inductively coupled plasma optical emission spectrometry (ICP-OES) (715-ES ICP analysis system; Varian). To prepare samples for ICP-OES measurements, the iridium and IrNi_{3.2} nanoparticles were dissolved in concentrated HCl 36% in the presence of NaClO₄ as an oxidizing agent using a microwave. Details of ICP-OES sample preparation can be found in the Supplementary Methods.

Electrochemical measurements. Electrochemical experiments were performed in a three-compartment glass cell with a rotating disk electrode (RDE) (5 mm in diameter of glassy carbon; Pine Instrument) and a potentiostat (Biologic) at room temperature. A platinum mesh and a Hg/Hg₂SO₄ electrode (in saturated K₂SO₄) were used as the counter and reference electrode, respectively. The Hg/Hg₂SO₄ electrode was calibrated against the RHE in H₂-saturated 0.05 M H₂SO₄ before electrochemical measurements. All electrochemical RDE measurements were carried out in N₂-saturated 0.05 M H₂SO₄ and repeated on three catalyst films for each catalyst. All potentials reported in this paper were normalized with respect to the RHE unless otherwise stated.

To prepare the working electrode, a certain amount of catalyst was suspended in 3.980 ml of ultrapure water (Millipore; 18 MΩ), 1.000 ml of isopropanol and 20 μl of 5 wt% Nafion solution with sonication for 15 min to form a uniform ink. Then, 10 μl of the ink was pipetted onto a pre-polished and cleaned glassy carbon electrode (RDE) and dried at 60 °C for 7 min in air, resulting in a thin uniform catalyst film. The amount of catalyst was calculated to obtain the final film on the glassy carbon electrode containing 10.2 μg_{Ir} cm⁻².

The precursor alloy nanoparticles were dealloyed and oxidized by applying potential cycling from +0.05 to +1.5 V_{RHE} for 50 cycles with a scan rate of 500 mV s⁻¹. For comparison, identical electrochemical treatment was performed for the iridium nanoparticles. The electrocatalytic activities of the IrO_x and IrNiO_x nanoparticles were recorded using linear sweep voltammetry from +1.0 to +1.8 V_{RHE} with a scan rate of 5 mV s⁻¹ under an electrode rotation of 1,600 r.p.m. Potentiostatic electrochemical impedance spectroscopy was carried out before each OER measurement for iR correction. The iridium-mass-based OER activity was evaluated taking the iR- and capacity-corrected current normalized to the iridium mass on the electrode. The capacitance currents were evaluated by the mean value of the current in the potential range of 1.0 to 1.23 V_{RHE}, where no Faradaic process takes place. The surface-specific OER activity was evaluated taking the iR- and capacity-corrected current normalized to the number of electrochemically accessible iridium sites (intrinsic specific activities, j_{specific}) derived from the Ir^{III+}-Ir^{IV+} transition⁹.

Operando XAS measurements. Samples for operando XAS measurements were analysed in a custom-made in situ cell and potentiostat (Biologic) at room temperature. A platinum mesh and Ag/AgCl electrode (in 3 M KCl) were used as the counter and reference electrode, respectively. H₂SO₄ (0.05 M) was used as the electrolyte in all measurements. The Ag/AgCl electrode was calibrated against an RHE in H₂-saturated 0.05 M H₂SO₄ before the in situ measurements. The samples were prepared by drop-casting 10 times 10 μl of the identical ink composition, as described above, on carbon sheets (AvCarb P50T; Fuel Cell Store; ~10 mm × 50 mm). The final films contained about 0.1 mg of catalyst powder.

The iridium L₃-edge XANES and EXAFS data were collected at the 7T-WLS/1 μSpot beamline at the BESSY synchrotron radiation source operated by the Helmholtz-Zentrum Berlin. The XAS measurements were performed in fluorescence-transmission geometry, where the spectrum of the samples and standards were measured in fluorescence mode, and the spectrum of the reference material (metallic iridium) placed behind the sample was simultaneously measured in transmission mode. The reference spectra were used to align the sample spectra to rule out any systematic energy drifts over the course of the measurements. The general set-up is schematically depicted in Supplementary Fig. 2. All datasets were collected at room temperature.

An identical electrochemical oxidation step was applied, as for the previous electrochemical RDE measurements, for both pure iridium nanoparticles and

IrNi_{3.2} nanoparticles. The electrolyte was exchanged for fresh electrolyte after the electrochemical oxidation to remove the nickel ions dissolved in the solution during electrochemical oxidation. After the electrochemical oxidation, XAS was collected at 0.4, 1.38 and 1.5 V_{RHE} for each catalyst, starting with the lowest potential and stepping up to higher potentials. At each potential, the catalyst was allowed to be stabilized 5 min before XAS measurement and the potential was kept constant throughout the XAS measurement.

The XANES and EXAFS raw data were processed using the ATHENA program and EXAFS analysis was performed using the ARTEMIS program³⁴. The ab initio calculated phases and amplitudes were constructed by the program FEFF6 (ref. ³⁵) integrated in the ARTEMIS program, based on the rutile-type crystal structure of IrO₂⁴².

Under the assumption that the L₃:L₂ ratio remains fixed, which is reasonable for oxidized iridium²⁸, the integral area of the L₃ white line is proportional to the number of *d*-band holes^{28,56,57}. To identify Δd as a function of the applied potential, the L₃ edges were fit with an arctangent function, to account for the transition to continuum, and a Lorentzian function, to account for the transition to the bound state. The arctangent function was then subtracted from the experimental data to yield the white line intensity (see Supplementary Fig. 3). Considering the IrO_x sample, the integral area increased when the applied potential was increased from +0.4 to +1.38 V_{RHE} (see Supplementary Fig. 4). This increase was due to the oxidation of iridium sites, as observed in the cyclic voltammogram (Supplementary Fig. 1d). The integrated white line area increased further under OER conditions (1.5 V_{RHE}) and became larger than that of IrO₂—despite the contribution of metallic iridium in the particle cores—indicating that iridium sites in IrO_x exhibited more 5*d*-band holes than the formally *iv*+ state of rutile-type IrO₂. However, the assigned oxidation state of iridium in rutile-type IrO₂ is based on conventional oxidation state rules, but Bader and Voronoi analyses of the computed charge density respectively suggest that there is only 51 or 63% ionic character due to the high degree of covalency. Thus, the iridium ions in crystalline IrO₂ may not even reach an absolute *iv*+ oxidation state, although in this work we refer to it as such for the sake of simplicity.

For the IrNiO_x sample, the absolute value of the integrated white line area is smaller than that of IrO_x, probably due to the influence of the metallic core. This influence of the metallic core cannot be removed by deconvolution of the white line, as the multiple bound states accessible to transitions from the iridium 2*p* lead to a large number of adjustable parameters in the fitting procedure. This allows for a variety of fit solutions, preventing a unique meaningful deconvolution of the edge spectral features²⁹. The influence of the metallic core can instead be lessened by turning to the energy position of the white line determined by the minimum of the second derivative of the normalized XANES spectra (see Supplementary Fig. 5). This is because, in the second derivative analysis, the arctangent amplitude becomes negligible, whereas the second derivative of the positive Lorentzian is a negative-going peak with the same relative intensity and position as the original Lorentzian²⁹, allowing accurate determination of the white line position. This accepted analysis technique is described and applied in detail, for instance, by Choy et al.^{29,30}. For the metallic iridium oxides studied herein, such an analysis will become ambiguous in the case of a reverse iridium 2*p* core level shift, such as that exhibited for Ir^{III+} and Ir^{IV+} in photoemission at the N_{6,7} edge^{20,46}. However, as the integrated white line intensity clearly demonstrates oxidation of iridium beyond the formal Ir^{IV+} of rutile-type IrO₂, we can be confident that changes in the energy position associated with increasing the applied potential are linked to increasing the number of *d*-band holes. Thus, given the complexity of the present iridium oxide compounds, we are confident that the second derivative method is the most appropriate way to analyse the experimental XANES spectra.

DFT calculations. All DFT calculations were performed with the Quantum ESPRESSO package version 6.1 (ref. ³⁹) using the Perdew–Burke–Ernzerhof exchange and correlation potential⁶⁰ as it recovers the correct ground state of rutile-type IrO₂⁵¹. Projector-augmented wave datasets from the PS Library⁶² were used with a kinetic energy cut-off of 90 Ry and a charge density cut-off of 900 Ry. A *k*-point mesh equivalent to at least (12 × 12 × 16) for the crystallographic unit cell of rutile-type IrO₂ was used with Marzari–Vanderbilt cold smearing⁶³, with a smearing parameter of 0.02 Ry. All structures were computed by relaxing the cell volume/shape and ionic positions, except for the iridium and oxygen in the vacancy-rich rutile-type and hollandite-type Ir₃O₈ (Supplementary Fig. 9h,i). Defect structures were prepared by introducing iridium vacancies to rutile-type and hollandite-type IrO₂. The vacancy density was varied to see how the electron holes introduced by vacancy formation were distributed across iridium and oxygen. A final self-consistent field calculation was performed to ensure the pressure was below 0.5 kbar. A Löwdin population analysis was performed to capture the orbital angular momentum resolved partial charges reported in the manuscript. The Cartesian coordinates of the 3D model can be found in the Supplementary Data.

Resonant high-energy synchrotron XRD experiments. Pure iridium, IrNi_{3.2} precursor alloy and electrochemically treated IrO_x and IrNiO_x nanoparticles were subjected to resonant (HE-XRD) experiments at the 1-ID-C beamline of the Advanced Photon Source, Argonne. Samples were sealed in thin-walled glass

capillaries and measured in transmission geometry. An empty glass capillary and carbon powder alone were measured separately. The experimental set-up was calibrated with high-purity standard silicon powder. Two sets of HE-XRD patterns for each of the foregoing nanoparticles were collected using X-rays of different energy. One of the sets was collected using X-rays with an energy of 76,087 keV, which is 24 eV below the K adsorption edge of iridium (76,111 keV). The other was collected using X-rays with an energy of 75,811 keV, which is 300 eV below the K edge of iridium. X-rays were delivered by a combination of a bent double-Laue monochromator, collimating refracting lenses and a four-crystal high-energy resolution ($\Delta E = 8$ eV) monochromator. Scattered X-ray intensities were collected by a solid-state germanium detector coupled to a multi-channel analyser. The experimental set-up is shown in Supplementary Fig. 10a. A few energy windows, covering several neighbouring channels, were set up to obtain X-ray intensities integrated over specific X-ray energy ranges during the data collection, as exemplified in Supplementary Fig. 10b,c. The energy windows covered: the coherent intensities only; the coherent, Compton and iridium K_{β} fluorescence intensities all together; the iridium $K_{\alpha 1}$ and $K_{\alpha 2}$ fluorescence; and the total intensities scattered into the germanium detector. HE-XRD patterns for the respective nanoparticles were collected several times, scanning up to wave vectors, q , of 25 \AA^{-1} and then averaged to improve the statistical accuracy. XRD patterns for IrNiO_x nanoparticles are shown in Supplementary Fig. 10c as an example. As can be seen in the figure, the patterns show a few distinct Bragg-like peaks at low diffraction angles and several broad features at high diffraction angles; that is, they are rather diffuse in nature. This rendered sharp-Bragg-peak-based techniques for determining the 3D atomic structure of bulk metals and alloys difficult to apply in the case of the nanoparticles studied here. Hence, HE-XRD patterns were analysed in terms of total and iridium differential atomic PDFs. By definition, total PDFs reflect all atomic pair correlations in the studied nanoparticles; hence, the total atomic PDF for pure iridium nanoparticles reflects correlations between pairs of iridium atoms alone, while the total atomic PDF for IrNiO_x nanoparticles is a weighted sum of six partial atomic PDFs, $G_{\text{Ir}}(r): G_{\text{Ir-Ir}}(r), G_{\text{Ir-Ni}}(r), G_{\text{Ir-O}}(r), G_{\text{Ni-Ni}}(r), G_{\text{Ni-O}}(r)$ and $G_{\text{O-O}}(r)$. In contrast, differential atomic PDFs reflect atomic correlations specific to the atomic species whose edge was probed. In particular, the iridium differential atomic PDF shown in Fig. 5b and Supplementary Fig. 10d reflects only iridium-involving atomic pair correlations in the respective nanoparticles (that is, Ir–M (M = Ir or Ni) and Ir–O atomic pair correlations alone), thus providing extra sensitivity to Ir–O species, which are the driving force for the OER over the nanoparticles. More details of the resonant HE-XRD experiments and derivation of total and iridium differential atomic PDFs can be found in refs^{64–66} and the Supplementary Methods.

Data availability

The data that support the plots within this paper and other findings of this study are available from the corresponding authors upon reasonable request.

Received: 1 August 2018; Accepted: 30 August 2018;

Published online: 08 October 2018

References

- Dau, H. et al. The mechanism of water oxidation: from electrolysis via homogeneous to biological catalysis. *ChemCatChem* **2**, 724–761 (2010).
- Olah, G. A., Goepfert, A. & Prakash, G. K. S. Chemical recycling of carbon dioxide to methanol and dimethyl ether: from greenhouse gas to renewable, environmentally carbon neutral fuels and synthetic hydrocarbons. *J. Org. Chem.* **74**, 487–498 (2009).
- Suntivich, J., May, K. J., Gasteiger, H. A., Goodenough, J. B. & Shao-Horn, Y. A perovskite oxide optimized for oxygen evolution catalysis from molecular orbital principles. *Science* **334**, 1383–1385 (2011).
- Xu, J. et al. Oxygen evolution catalysts on supports with a 3-D ordered array structure and intrinsic proton conductivity for proton exchange membrane steam electrolysis. *Energy Environ. Sci.* **7**, 820–830 (2014).
- Reier, T., Nong, H. N., Teschner, D., Schlögl, R. & Strasser, P. Electrocatalytic oxygen evolution reaction in acidic environments—reaction mechanisms and catalysts. *Adv. Energy Mater.* **7**, 1601275 (2017).
- Reier, T., Oezaslan, M. & Strasser, P. Electrocatalytic oxygen evolution reaction (OER) on Ru, Ir, and Pt catalysts: a comparative study of nanoparticles and bulk materials. *ACS Catal.* **2**, 1765–1772 (2012).
- Cherevko, S. et al. Oxygen and hydrogen evolution reactions on Ru, RuO₂, Ir, and IrO₂ thin film electrodes in acidic and alkaline electrolytes: a comparative study on activity and stability. *Catal. Today* **262**, 170–180 (2016).
- Carmo, M., Fritz, D. L., Mergel, J. & Stolten, D. A comprehensive review on PEM water electrolysis. *Int. J. Hydrogen Energy* **38**, 4901–4934 (2013).
- Nong, H. N., Gan, L., Willinger, E., Teschner, D. & Strasser, P. IrO_x core-shell nanocatalysts for cost- and energy-efficient electrochemical water splitting. *Chem. Sci.* **5**, 2955–2963 (2014).
- Reier, T. et al. Molecular insight in structure and activity of highly efficient, low-Ir Ir–Ni oxide catalysts for electrochemical water splitting (OER). *J. Am. Chem. Soc.* **137**, 13031–13040 (2015).
- Seitz, L. C. et al. A highly active and stable IrO_x/SrIrO₃ catalyst for the oxygen evolution reaction. *Science* **353**, 1011–1014 (2016).
- Strasser, P. et al. Lattice-strain control of the activity in dealloyed core-shell fuel cell catalysts. *Nat. Chem.* **2**, 454–460 (2010).
- Zhang, Z. et al. One-pot synthesis of highly anisotropic five-fold-twinned PtCu nanoframes used as a bifunctional electrocatalyst for oxygen reduction and methanol oxidation. *Adv. Mater.* **28**, 8712–8717 (2016).
- Zhang, Z. et al. Submonolayered Ru deposited on ultrathin Pd nanosheets used for enhanced catalytic applications. *Adv. Mater.* **28**, 10282–10286 (2016).
- Fan, Z. et al. Synthesis of 4H/fcc-Au@M (M = Ir, Os, IrOs) core-shell nanoribbons for electrocatalytic oxygen evolution reaction. *Small* **12**, 3908–3913 (2016).
- Kötz, R., Neff, H. & Stucki, S. Anodic iridium oxide films: XPS studies of oxidation state changes and O₂ evolution. *J. Electrochem. Soc.* **131**, 72–77 (1984).
- Sanchez Casalongue, H. G. et al. In situ observation of surface species on iridium oxide nanoparticles during the oxygen evolution reaction. *Angew. Chem. Int. Ed.* **53**, 7169–7172 (2014).
- Mo, Y. et al. In situ iridium L_{III}-edge X-ray absorption and surface enhanced Raman spectroscopy of electrodeposited iridium oxide films in aqueous electrolytes. *J. Phys. Chem. B* **106**, 3681–3686 (2002).
- Hillman, A. R., Skopek, M. A. & Gurman, S. J. X-ray spectroscopy of electrochemically deposited iridium oxide films: detection of multiple sites through structural disorder. *Phys. Chem. Chem. Phys.* **13**, 5252–5263 (2011).
- Pfeifer, V. et al. The electronic structure of iridium oxide electrodes active in water splitting. *Phys. Chem. Chem. Phys.* **18**, 2292–2296 (2016).
- Lee, Y., Suntivich, J., May, K. J., Perry, E. E. & Shao-Horn, Y. Synthesis and activities of rutile IrO₂ and RuO₂ nanoparticles for oxygen evolution in acid and alkaline solutions. *J. Phys. Chem. Lett.* **3**, 399–404 (2012).
- Wang, C. et al. Synthesis of Cu–Ir nanocages with enhanced electrocatalytic activity for the oxygen evolution reaction. *J. Mater. Chem. A* **3**, 19669–19673 (2015).
- Lettenmeier, P. et al. Nanosized IrO_x–Ir catalyst with relevant activity for anodes of proton exchange membrane electrolysis produced by a cost-effective procedure. *Angew. Chem. Int. Ed.* **55**, 742–746 (2016).
- Grimaud, A. et al. Activation of surface oxygen sites on an iridium-based model catalyst for the oxygen evolution reaction. *Nat. Energy* **2**, 16189 (2016).
- Kodintsev, I. M., Trasatti, S., Rubel, M., Wieckowski, A. & Kautfer, N. X-ray photoelectron spectroscopy and electrochemical surface characterization of iridium(IV) oxide + ruthenium(IV) oxide electrodes. *Langmuir* **8**, 283–290 (1992).
- Diaz-Morales, O. et al. Iridium-based double perovskites for efficient water oxidation in acid media. *Nat. Commun.* **7**, 12363 (2016).
- Brown, M., Peierls, R. E. & Stern, E. A. White lines in X-ray absorption. *Phys. Rev. B* **15**, 738–744 (1977).
- Clancy, J. P. et al. Spin-orbit coupling in iridium-based 5d compounds probed by X-ray absorption spectroscopy. *Phys. Rev. B* **86**, 195131 (2012).
- Choy, J.-H., Kim, D.-K., Demazeau, G. & Jung, D.-Y. L_{III}-edge XANES study on unusually high valent iridium in a perovskite lattice. *J. Phys. Chem.* **98**, 6258–6262 (1994).
- Choy, J.-H., Kim, D.-K., Hwang, S.-H., Demazeau, G. & Jung, D.-Y. XANES and EXAFS studies on the Ir–O bond covalency in ionic iridium perovskites. *J. Am. Chem. Soc.* **117**, 8557–8566 (1995).
- Frazer, E. J. & Woods, R. The oxygen evolution reaction on cycled iridium electrodes. *J. Electroanal. Chem.* **102**, 127–130 (1979).
- Conway, B. E. & Mozota, J. Surface and bulk processes at oxidized iridium electrodes II. Conductivity-switched behaviour of thick oxide films. *Electrochim. Acta* **28**, 9–16 (1983).
- Mozota, J. & Conway, B. E. Surface and bulk processes at oxidized iridium electrodes I. Monolayer stage and transition to reversible multilayer oxide film behaviour. *Electrochim. Acta* **28**, 1–8 (1983).
- Cherevko, S. et al. Stability of nanostructured iridium oxide electrocatalysts during oxygen evolution reaction in acidic environment. *Electrochem. Commun.* **48**, 81–85 (2014).
- Reier, T. et al. Electrocatalytic oxygen evolution on iridium oxide: uncovering catalyst–substrate interactions and active iridium oxide species. *J. Electrochem. Soc.* **161**, F876–F882 (2014).
- Lengke, M. F. et al. Mechanisms of gold bioaccumulation by filamentous cyanobacteria from gold(III)–chloride complex. *Environ. Sci. Technol.* **40**, 6304–6309 (2006).
- Rand, D. A. J. & Woods, R. Cyclic voltammetric studies on iridium electrodes in sulphuric acid solutions: nature of oxygen layer and metal dissolution. *J. Electroanal. Chem. Interfacial Electrochem.* **55**, 375–381 (1974).
- Rand, D. A. J., Michell, D. & Woods, R. Cyclic voltammetric studies on iridium electrodes in sulphuric acid solutions: nature of oxygen layer and metal dissolution. In *Proc. Symposium on Electrode Materials and Processes for Energy Conversion and Storage* (eds McIntyre, J. D. E., Srinivasan, S. & Will, F. G.) 217–233 (Electrochemical Society, 1977).

39. Görlin, M. et al. Oxygen evolution reaction dynamics, Faradaic charge efficiency, and the active metal redox states of Ni–Fe oxide water splitting electrocatalysts. *J. Am. Chem. Soc.* **138**, 5603–5614 (2016).
40. Shannon, R. Revised effective ionic radii and systematic studies of interatomic distances in halides and chalcogenides. *Acta Cryst.* **32**, 751–767 (1976).
41. Abbott, D. F. et al. Iridium oxide for the oxygen evolution reaction: correlation between particle size, morphology, and the surface hydroxo layer from operando XAS. *Chem. Mater.* **28**, 6591–6604 (2016).
42. Bolzan, A. A., Fong, C., Kennedy, B. J. & Howard, C. J. Structural studies of rutile-type metal dioxides. *Acta Cryst.* **53**, 373–380 (1997).
43. Arikawa, T., Takasu, Y., Murakami, Y., Asakura, K. & Iwasawa, Y. Characterization of the structure of RuO₂–IrO₂/Ti electrodes by EXAFS. *J. Phys. Chem. B* **102**, 3736–3741 (1998).
44. Shannon, R. D. & Vincent, H. *Relationships Between Covalency, Interatomic Distances, and Magnetic Properties in Halides and Chalcogenides* (Springer, Berlin & Heidelberg, 1974).
45. Willinger, E., Massué, C., Schlögl, R. & Willinger, M. G. Identifying key structural features of IrO₂ water splitting catalysts. *J. Am. Chem. Soc.* **139**, 12093–12101 (2017).
46. Weber, D. et al. Trivalent iridium oxides: layered triangular lattice iridate K_{0.75}Na_{0.25}IrO₂ and oxyhydroxide IrOOH. *Chem. Mater.* **29**, 8338–8345 (2017).
47. Ushakov, A. V., Streltsov, S. V. & Khomskii, D. I. Crystal field splitting in correlated systems with negative charge-transfer gap. *J. Phys. Condens. Matter.* **23**, 445601 (2011).
48. Nørskov, J. K. et al. Origin of the overpotential for oxygen reduction at a fuel-cell cathode. *J. Phys. Chem. B* **108**, 17886–17892 (2004).
49. Pfeifer, V. et al. In situ observation of reactive oxygen species forming on oxygen-evolving iridium surfaces. *Chem. Sci.* **8**, 2143–2149 (2017).
50. Betley, T. A., Wu, Q., Van Voorhis, T. & Nocera, D. G. Electronic design criteria for O–O bond formation via metal–oxo complexes. *Inorg. Chem.* **47**, 1849–1861 (2008).
51. Mavros, M. G. et al. What can density functional theory tell us about artificial catalytic water splitting? *Inorg. Chem.* **53**, 6386–6397 (2014).
52. Fierro, S., Nagel, T., Baltruschat, H. & Comninellis, C. Investigation of the oxygen evolution reaction on Ti/IrO₂ electrodes using isotope labelling and on-line mass spectrometry. *Electrochem. Commun.* **9**, 1969–1974 (2007).
53. Strasser, P. Free electrons to molecular bonds and back: closing the energetic oxygen reduction (ORR)–oxygen evolution (OER) cycle using core–shell nanoelectrocatalysts. *Acc. Chem. Res.* **49**, 2658–2668 (2016).
54. Ravel, B. & Newville, M. ATHENA, ARTEMIS, HEPHAESTUS: data analysis for X-ray absorption spectroscopy using IFEFFIT. *J. Synchrotron Rad.* **12**, 537–541 (2005).
55. Zabinsky, S. I., Rehr, J. J., Ankudinov, A., Albers, R. C. & Eller, M. J. Multiple-scattering calculations of X-ray-absorption spectra. *Phys. Rev. B* **52**, 2995–3009 (1995).
56. Horsley, J. A. Relationship between the area of L_{2,3} X-ray absorption edge resonances and the *d* orbital occupancy in compounds of platinum and iridium. *J. Chem. Phys.* **76**, 1451–1458 (1982).
57. Starace, A. F. Potential-barrier effects in photoabsorption. I. General theory. *Phys. Rev. B* **5**, 1773–1784 (1972).
58. Lytle, F. W. & Gregor, R. B. Investigation of the “join” between the near edge and extended X-ray absorption fine structure. *Appl. Phys. Lett.* **56**, 192–194 (1990).
59. Giannozzi, P. et al. QUANTUM ESPRESSO: a modular and open-source software project for quantum simulations of materials. *J. Phys. Condens. Matter.* **21**, 395502 (2009).
60. Perdew, J. P., Burke, K. & Ernzerhof, M. Generalized gradient approximation made simple. *Phys. Rev. Lett.* **77**, 3865–3868 (1996).
61. Ping, Y., Galli, G. & Goddard, W. A. Electronic structure of IrO₂: the role of the metal *d* orbitals. *J. Phys. Chem. C* **119**, 11570–11577 (2015).
62. Dal Corso, A. Pseudopotentials periodic table: from H to Pu. *Comput. Mater. Sci.* **95**, 337–350 (2014).
63. Marzari, N., Vanderbilt, D., De Vita, A. & Payne, M. C. Thermal contraction and disordering of the Al(110) surface. *Phys. Rev. Lett.* **82**, 3296–3299 (1999).
64. Fuoss, P. H., Eisenberger, P., Warburton, W. K. & Bienenstock, A. Application of differential anomalous X-ray scattering to structural studies of amorphous materials. *Phys. Rev. Lett.* **46**, 1537–1540 (1981).
65. Petkov, V. & Shastri, S. D. Element-specific structure of materials with intrinsic disorder by high-energy resonant X-ray diffraction and differential atomic pair-distribution functions: a study of PtPd nanosized catalysts. *Phys. Rev. B* **81**, 165428 (2010).
66. Waseda, Y. *Anomalous X-Ray Scattering for Materials Characterization: Atomic-Scale Structure Determination* (Springer, 2002).
67. Momma, K. & Izumi, F. VESTA 3 for three-dimensional visualization of crystal, volumetric and morphology data. *J. Appl. Crystallogr.* **44**, 1272–1276 (2011).

Acknowledgements

We thank the Zentraleinrichtung für Elektronenmikroskopie of the Technische Universität Berlin for support with the TEM technique and R. Loukrakpam for recording the TEM micrographs. Financial support from the German Research Foundation through grant STR 596/3-1/-2 under Priority Program 1613 is gratefully acknowledged. We thank the Helmholtz-Zentrum Berlin for allocation of synchrotron radiation beamtime under the proposal 14201762-ST/R, I. Zizak for technical support at the μ Spot beamline of BESSY, A. Bergmann (Fritz Haber Institute of the Max Planck Society) for contributing to data collection at BESSY and S. Shastri (APS, Argonne National Laboratory) for helping with the HE-XRD measurements. This work was supported in part by DOE-BES grant DE-SC0006877. The work also used resources of the Advanced Photon Source at the Argonne National Laboratory provided by the DOE Office of Science under contract number DE-AC02-06CH11357. We acknowledge the Höchstleistungsrechenzentrum Stuttgart for access to the supercomputer Hazel Hen. T.J. acknowledges the Alexander von Humboldt Foundation for financial support.

Author contributions

P.S. and H.N.N. conceived and designed the experiments. H.N.N. carried out the chemical synthesis and electrochemical experiments, and analysed the results. H.N.N., T.R. and H.-S.O. performed the operando XAS experiments. H.N.N. analysed the XAS data. V.P. carried out the resonant HE-XRD measurements and analysed the data. M.G. acquired the TEM images. T.J. carried out the DFT calculations. P.P. and M.H. performed the STEM-EDX measurements. H.N.N., P.S., T.J. and V.P. wrote the manuscript. All authors discussed the results, drew conclusions and commented on the manuscript.

Competing interests

The authors declare no competing interests.

Additional information

Supplementary information is available for this paper at <https://doi.org/10.1038/s41929-018-0153-y>.

Reprints and permissions information is available at www.nature.com/reprints.

Correspondence and requests for materials should be addressed to T.J. or P.S.

Publisher's note: Springer Nature remains neutral with regard to jurisdictional claims in published maps and institutional affiliations.

© The Author(s), under exclusive licence to Springer Nature Limited 2018